Effect of longitudinal modulation on Alfvén wave filamentation

Thierry Passot,[1] Catherine Sulem,[2] and Pierre-Louis Sulem[1]
[1] *Observatoire de la Côte d'Azur, Boîte Postale 229, 06304 Nice Cedex 4, France*
[2] *Department of Mathematics, University of Toronto, Toronto, Canada M5S 1A1*
(Received 22 February 1994)

The modulation of circularly polarized Alfvén waves due to quasitransverse perturbations is addressed, and the nonlinear dynamics simulated numerically. In some instances, radial collapse (filamentation) of Alfvén waves can be arrested by the magnetosonic waves stirred by the ponderomotive force. Such waves may, however, develop sharp fronts leading to strong hydrodynamic effects.

PACS number(s): 52.35.Bj, 52.35.Mw, 02.30.Mv, 94.30.Tz

I. INTRODUCTION

The dynamics of a plasma subject to an ambient magnetic field is the object of a great deal of interest in various astrophysical and geophysical contexts such as the interstellar medium or the solar wind. Because of the consequences for the transport properties and the energy budget, an important question is whether the dynamics in such media is dominated by the propagation of nonlinear Alfvén waves (together with negligible hydrodynamic effects) or, if at the opposite, a truly magnetohydrodynamic (MHD) compressible turbulence can develop. In the interstellar medium for example, supersonic (and sub-Alfvénic) motions are observed at the scale of molecular clouds but the existence of a strong compressible turbulence where a significant dissipation occurs in shocks, could hardly be explained by the presently known mechanisms of energy injection [1]. Furthermore, the question arises of the origin of large density fluctuations at the scale of diffuse interstellar clouds.

In the earth bow shock, there is experimental evidence of the presence of almost circularly polarized Alfvén waves. Important density fluctuations are also observed, shifted with respect to the maximum wave intensity. Such fluctuations seem to originate from the ponderomotive force due to modulationally unstable wave trains. Furthermore, as observed by Spangler *et al.* [2], the amplitude of the fluctuations in the ambient field-aligned component of the Alfvén wave, appear to be larger than could be attributed to oblique propagation alone, given the constraints on the propagation angle. These authors suggest that the most likely explanation for the such relatively large fluctuations is that they arise as the consequence of transverse modulation.

As a first step towards the understanding of the basic nonlinear phenomena entering these problems, we study in this paper the three-dimensional modulational stability of Alfvén waves, propagating parallel to the ambient magnetic field, when coupled to low-frequency magnetosonic waves. In the weakly nonlinear regime, the interaction of a high-frequency to a low-frequency acoustic-type wave is usually governed by the Zakharov-Rubenchik equations [3]. In the specific case where the high-frequency wave is an Alfvén wave, the anisotropy of the system due to the ambient magnetic field, together with the presence of an additional (slow magnetosonic) wave, leads to a modified system of amplitude equations derived in Ref. [4]. These equations are the starting point of this paper. Of particular interest is the possible development of wave collapse and fronts. Although the validity of the amplitude equations breaks down near such singularities, these structures correspond to regions where significant heating (not included in the equations) may take place.

II. ENVELOPE EQUATIONS FOR ALFVÉN AND MAGNETOSONIC WAVES

A plasma where electron inertia together with ion-neutral friction are neglected and electric quasineutrality is assumed, can be described by the one-fluid equations where the Hall effect is retained (dispersive MHD)

$$\partial_t \rho + \nabla \cdot (\rho \mathbf{u}) = 0, \tag{2.1}$$

$$\rho(\partial_t \mathbf{u} + \mathbf{u} \cdot \nabla \mathbf{u}) = -\frac{\beta}{\gamma} \nabla \rho^\gamma + (\nabla \times \mathbf{b}) \times \mathbf{b}, \tag{2.2}$$

$$\partial_t \mathbf{b} - \nabla \times (\mathbf{u} \times \mathbf{b}) = -\frac{1}{R_i} \nabla \times \left[\frac{1}{\rho} (\nabla \times \mathbf{b}) \times \mathbf{b} \right], \tag{2.3}$$

$$\nabla \cdot \mathbf{b} = 0. \tag{2.4}$$

The parameter β is the square ratio of the velocities of sonic and Alfvén waves, γ denotes the polytropic gas constant and R_i the nondimensional gyromagnetic frequency of the ions.

Equations (2.1)–(2.4) admit exact solutions in the form of circularly polarized Alfvén waves whose amplitude is here assumed to be small. A modulation analysis starting directly from these equations is feasible but, when the wavelength of the carrying Alfvén wave is large compared to the gyromagnetic radius of the ions, it is easier to start from a multidimensional version of the derivative nonlinear Schrödinger (DNLS) equation [5], in which the coupling to the magnetosonic waves (relevant when dealing with multidimensional Alfvén wave trains), has been included [4]. A derivation of the modulation equations

in this context, is also presented in Ref. [4], using a systematic multiple-scale method. They read

$$\frac{1}{i}\left(\partial_T B + \frac{v_g}{\mu}\partial_X B\right) + k\left(V + \frac{\hat{\rho}}{2} + \frac{\bar{a}}{2}\right)B - \frac{1}{4k(1-\beta)}\Delta_\perp B + \frac{1}{2R_i}\partial_{XX}B = 0, \quad (2.5)$$

$$\partial_T \hat{\rho} + \frac{1}{\epsilon\mu}\partial_X V = 0, \quad (2.6)$$

$$\partial_T V - \frac{2}{\epsilon\mu}\partial_X V = \frac{\partial_X}{\epsilon\mu}\left[(1-\beta)\hat{\rho} - \beta\bar{a} - \frac{|B|^2}{2}\right] + \frac{i}{4k(1-\beta)}\left(B^*\Delta_\perp B - B\Delta_\perp B^*\right), \quad (2.7)$$

$$\frac{2k}{R_i}\partial_{XX}\bar{a} + \Delta_\perp\left(\beta\hat{\rho} + (1+\beta)\bar{a} + \frac{|B|^2}{2}\right) = 0\,. \quad (2.8)$$

Here B denotes the (complex) envelope of the transverse magnetic field and $\bar{a}$ the slowly varying component (referred to as the mean value) of the longitudinal magnetic field. The quantities V and $\hat{\rho}$ are defined in terms of the mean longitudinal velocity u_x and the mean density ρ of the fluid by $V = \bar{a} - \rho + u_x$ and $\hat{\rho} = \rho - \bar{a}$. The wave number of the carrying Alfvén wave is ϵk (with $\epsilon \ll 1$) and the group velocity (in a reference frame moving at the phase velocity) is $v_g = -k/R_i$. The other small parameter μ measures the wave amplitude and thus the inverse scale of the modulation.

Equations (2.5)–(2.8) appear as a uniform description, obtained by matching two asymptotic regimes related to the ratio of typical transverse and longitudinal scales. In the "inner" region (perturbations quasitransverse to the Alfvén wave propagation) where the full dynamics of density waves is retained, the mean flow term $\frac{i}{4k(1-\beta)}\left(B^*\Delta_\perp B - B\Delta_\perp B^*\right)$ in Eq. (2.7), can in fact be replaced by $\partial_T|B|^2$ as seen from Eq. (3.43) of Ref. [4]. In the "outer" region, this term is subdominant. It vanishes exactly for purely longitudinal perturbations, a case where we recover the equations given in Ref. [6]. In a uniform formulation, it is thus legitimate to replace the mean flow term by $\partial_T|B|^2$ in both regions. As shown later, such a replacement introduces subdominant corrections which restore the Hamiltonian character of the problem. Furthermore, the term $\frac{2k}{R_i}\partial_{XX}\bar{a}$ in (2.8), which is relevant only in the outer domain, results from an "adiabatic" approximation, usual in the context of Davey-Stewartson equations. As stressed in Ref. [7], it may however be useful, especially when Eq. (2.8) is of hyperbolic type ($k < 0$), to retain in this equation a derivative with respect to a faster time scale. In the reference frame used here, this consists in replacing $2\mu\partial_{XX}\bar{a}$ by $2\mu\partial_{XT}\bar{a}$ in (2.8).

In this paper, we are mainly interested in quasitransverse perturbations (filamentation instability [8], [9]). It is thus convenient to use rescaled variables $X = \mu R_i X$, $(\tilde{Y}, \tilde{Z}) = 2|k|\sqrt{|1-\beta|}(Y, Z)$ and $\tilde{T} = |k|T$, adapted to slow variations in the longitudinal direction, that still retain the effect of the group velocity. After dropping the tilde, hat, and bar symbols and defining $\eta = \epsilon|k|/R_i$ and $\xi = \mu\sqrt{R_i/2|k|}$, we get

$$i(\partial_T B - \kappa\partial_X B) - \kappa\left(V + \frac{\rho}{2} + \frac{a}{2}\right)B + \sigma\kappa\Delta_\perp B - \xi^2\partial_{XX}B = 0, \quad (2.9)$$

$$\eta\partial_T\rho + \partial_X V = 0, \quad (2.10)$$

$$\eta\partial_T V - 2\partial_X V - (1-\beta)\partial_X\rho + \beta\partial_X a = (\eta\partial_T - \tfrac{1}{2}\partial_X)|B|^2, \quad (2.11)$$

$$\xi^2\partial_{XT}a + |1-\beta|\Delta_\perp\left(\beta\rho + (1+\beta)a + \frac{|B|^2}{2}\right) = 0\,, \quad (2.12)$$

with $\kappa = \mathrm{sgn}(k)$ and $\sigma = \mathrm{sgn}(1-\beta)$. In this formulation, the modulation equations admit an Hamiltonian

$$\mathcal{H} = \int\left\{\sigma|\nabla_\perp B|^2 - \kappa\xi^2|\partial_X B|^2\right\}d^3\mathbf{r} + \int\left\{\frac{1}{2}[(\beta-1)\rho^2 + V^2 + (1+\beta)a^2 + 2\beta a\rho + (a+\rho)|B|^2]\right\}d^3\mathbf{r}\,. \quad (2.13)$$

When linearized, Eqs. (2.10)–(2.12) describe three magnetosonic waves: the ion-acoustic waves whose phase velocities identify to $-1\pm\sqrt{\beta}$, and the magnetosonic wave which propagates with the same velocity as the Alfvén wave. Related equations were derived in Ref. [10] for ion-cyclotron waves, coupled to the four magnetosonic waves. In the present asymptotics, where the wavelength of the carrying wave is large compared to the ion gyromagnetic radius, the magnetosonic wave propagating backward with the Alfvén wave velocity is subdominant at the retained scales.

The modulation Eqs. (2.9)–(2.12) couple various effects that deserve a separate investigation before a comprehensive analysis of the Alfvén wave problem be carried out. For example, when $\sigma\kappa = +1$, the second order spatial operator in Eq. (2.9) is hyperbolic. In this case, even in the simpler context of the nonlinear Schrödinger equation, new phenomena like splitting can occur [11]. When sonic waves are treated in the adiabatic limit (valid for nonquasitransverse modulations), Eqs. (2.9)–(2.12) reduce to a Davey-Stewartson-type equation [15]. Formation of singularities for Davey-Stewartson equations is discussed in Ref. [12] when the equation for the potential is of elliptic type, the other case being mostly open [13], [14]. After presenting in the next section a linear modulational stability analysis of a plane Alfvén wave,

we concentrate on the nonlinear dynamics in the weak dispersion limit.

III. MODULATIONAL STABILITY

Equations (2.9)–(2.12) admit solutions of the form $\rho = V = a = 0$ and $B = b_0$. In order to study their modulational stability, we write the perturbed field $B = b_0(1+b)e^{i\phi}$. Linearizing the system and considering perturbations ρ, V, a, b, and ϕ proportional to $e^{i(\mathbf{K}\cdot\mathbf{r}-\Omega T)}$ with $\mathbf{K} = (K_x, \mathbf{K}_\perp)$, we obtain the dispersion relation ($K_\perp = |\mathbf{K}_\perp|$)

$$\begin{vmatrix} A & B & 0 & 0 & 0 \\ -B & A & \frac{\kappa}{2} & \kappa & \frac{\kappa}{2} \\ 0 & 0 & -\eta\Omega & K_x & 0 \\ C & 0 & -(1-\beta)K_x & -(\eta\Omega+2K_x) & \beta K_x \\ D & 0 & -\sigma\beta(1-\beta)K_\perp^2 & 0 & E \end{vmatrix} = 0 ,$$

where $A = -(i\Omega + i\kappa K_x)$, $B = \xi^2 K_x^2 - \sigma\kappa K_\perp^2$, $C = |b_0|^2(K_x + 2\eta\Omega)$, $D = -|b_0|^2\sigma(1-\beta)K_\perp^2$ and $E = \xi^2\Omega K_x - \sigma(1-\beta^2)K_\perp^2$. We computed numerically the roots of this fifth-order polynomial in Ω for various values of the parameters. Two limiting cases are of interest, according to the ratio ξ/η.

We first address the regime $\eta \ll \xi$. Figure 1 displays the contours of the growth rate of the most unstable mode as a function of the angle $\theta = \arctan\frac{K_\perp}{K_x}$ and of β, for $\xi = 0.5$ and $\eta = 10^{-2}$. On the left-hand side, the pictures correspond to $\kappa = -1$ and on the right-hand side to $\kappa = +1$. On the top, they refer to the range $1.1 < \beta < 50$, and on the bottom to $0.01 < \beta < 0.9$. The neighborhood of $\beta = 1$ which deserves a special treatment, is avoided. Dotted lines delimit regions where Ω is real (no instability). The boundary layer obtained for $\beta > 1$ and θ close to $\pi/2$ has a thickness that decreases with η and corresponds to the transverse instability mentioned in Ref. [4]. For moderate values of β, the smallest critical stability angle appears to be β independent for $\sigma\kappa = +1$ [Figs. 1(a) and (d)]. In the other pictures, the curvature of the limiting lines at small angle is due to the nonadiabatic correction ($\partial_{XT}a$ instead of $\partial_{XX}a$) in Eq. (2.12). This line, which for any value of β is pushed towards smaller angles as ξ is decreased, was the only stability transition (except for purely transverse perturbations) occurring in the adiabatic limit considered in Ref. [4]. Here new regions are delimited. The additional curve in Fig. 1(a) is pushed towards larger β and smaller angles as η decreases. It moves towards smaller β as ξ diminishes. In contrast, the largest transition angle remains mostly unchanged. In both Figs. 1(b) and 1(c), the unstable range is pushed towards smaller angles as ξ is decreased. An interesting effect is observed for $\sigma = -1$ and $\kappa = +1$ [Fig. 1(b)] where, as η is decreased, the left-hand limiting curve straightens towards the curve obtained in the adiabatic limit corresponding to the replacement of $\partial_{XX}a$ by $\partial_{XT}a$ in Eq. (2.12). For both Figs. 1(b) and 1(c), the right-hand-side delimiting curve also has a limit when $\eta \to 0$. Furthermore, if the perturbation wave number K is also decreased, the unstable region extends to larger angles, confining the stability region to another boundary layer.

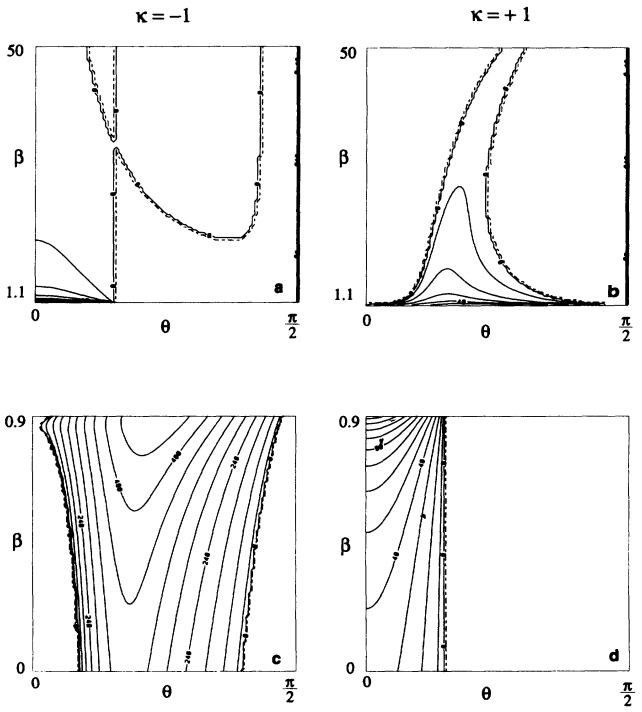

FIG. 1. Contours of the growth rate of the most unstable mode as a function of the direction $\theta = \arctan\frac{K_\perp}{K_x}$ of the modulation wave number, and of the parameter β. (a) Right-hand polarized Alfvén wave ($\kappa < 0$) with $\beta > 1$; (b) left-hand polarized Alfvén wave ($\kappa > 0$) with $\beta > 1$; (c) same polarization as (a) with $\beta < 1$; (d) same polarization as (b) with $\beta < 1$.

In the other limit ($\xi \ll \eta$), the stability diagrams greatly simplify. For a given value of η, the stability only depends on θ, κ, and σ. For $\sigma = \kappa = -1$, three regions are encountered when θ is increased, namely an instable one, a stable one, and the already mentioned unstable boundary layer near $\theta = \pi/2$. For $\sigma = -1$ and $\kappa = +1$, the system is unstable in the boundary layer only. For $\sigma = +1$ and $\kappa = -1$, it is always stable, while for $\sigma = \kappa = +1$ the stability diagram is similar to that of Fig. 1(d). In all the cases, the instability ranges (except the boundary layer about $\theta = \pi/2$) are pushed to smaller angles when η is decreased.

IV. SMALL DISPERSION LIMIT

The limit consisting in neglecting the terms proportional to ξ in Eqs. (2.9)–(2.12), corresponds to a situation where the modulation is at a much larger scale in the longitudinal than in the transverse directions. This leads to neglect the dispersion in Eq. (2.9) and to solve Eq. (2.12) in the form $a = \frac{-1}{1+\beta}(\frac{|B|^2}{2} + \beta\rho)$, up to a possible function of X and T that can be absorbed in a phase factor when a is substituted in Eq. (2.9). The equations then reduce to the inner limit (3.40)–(3.43) of Ref. [4]. Diagonalizing the linear part of the wave equations (assuming $\beta \neq 0$), and using a reference frame moving with the Alfvén group velocity, we get

$$i\partial_T B - (|B|^2 + W_1 + W_2)B + \sigma\Delta_\perp B = 0, \quad (4.1)$$

$$\eta\partial_T W_i + (\lambda_i + \eta\kappa)\partial_X W_i = \mu_i \partial_X |B|^2 \quad (i = 1, 2)\ , \quad (4.2)$$

with

$$V = |B|^2 + \frac{1}{\lambda_2 - \lambda_1}(\lambda_1 W_1 + \lambda_2 W_2), \quad (4.3)$$

$$\rho = \frac{1}{\lambda_2 - \lambda_1}(W_1 + W_2), \quad (4.4)$$

$$\lambda_1 = -1 - \sqrt{\frac{\beta}{1+\beta}}, \quad (4.5)$$

$$\lambda_2 = -1 + \sqrt{\frac{\beta}{1+\beta}}, \quad (4.6)$$

$$\mu_1 = \frac{-1}{\lambda_2 - \lambda_1}\left(\lambda_1 + \frac{1}{2(1+\beta)}\right) \times \left(\lambda_2 + \frac{4\beta+3}{2(1+\beta)}\right)\left(\frac{4(1+\beta)}{4\beta+3}\right), \quad (4.7)$$

$$\mu_2 = \frac{1}{\lambda_2 - \lambda_1}\left(\lambda_2 + \frac{1}{2(1+\beta)}\right) \times \left(\lambda_1 + \frac{4\beta+3}{2(1+\beta)}\right)\left(\frac{4(1+\beta)}{4\beta+3}\right)\ . \quad (4.8)$$

Note that we took $\kappa = 1$ in Eq. (4.1), since the case $\kappa = -1$ is recovered by replacing B by its complex conjugate. Furthermore, it is easily checked that

$$\frac{\mu_1}{\lambda_1} + \frac{\mu_2}{\lambda_2} + 1 = 0\ , \quad (4.9)$$

a condition which reflects the degeneracy observed in Ref. [15] when $\xi = \eta = 0$. The introduction of the W_1 and W_2 functions in Eq. (4.3) also splits the ponderomotive force $(\eta\partial_T - \frac{1}{2}\partial_X)|B|^2$ into a temporal contribution included in the potential of the envelope equation and a spatial contribution which stirs magnetosonic waves (see also Ref. [17] for a discussion of the relative importance of the two effects).

The variation with β of the coefficients λ_i and μ_i $(i = 1, 2)$ defined in (4.5)–(4.8) and entering Eqs. (4.1) and (4.2), is displayed in Fig. 2. We observe that $|\mu_2|$ decreases rapidly when β increases. For example, $\mu_2 = -8.3\times10^{-3}$ for $\beta = 0.5$ and $\mu_2 = -4.6\times10^{-4}$ for $\beta = 1.5$. Practically, as soon as β exceeds a few tenths (still avoiding the neighborhood of $\beta = 1$), we can discard the wave W_2 and take $\mu_1 = -\lambda_1$. Only one parameter $\epsilon_2 = \eta/\mu_1$ (assumed to be small) then remains explicitly in the equations. A second parameter is in fact provided by the ratio of the longitudinal to the transverse scales of the initial conditions. It is equivalent to fix these scales at order unity and, by a rescaling of the longitudinal coordinate, to replace Eqs. (4.1) and (4.2) by

$$i\partial_T B - (|B|^2 + W)B + \sigma\Delta_\perp B = 0, \quad (4.10)$$

$$\epsilon_1\partial_T W - c\partial_X W = \partial_X |B|^2\ , \quad (4.11)$$

where $c = (1 - \epsilon_2\kappa)$. Note that ϵ_1 can be chosen at will, the limit of purely transverse perturbations being recovered as ϵ_1 tends to infinity.

A linear modulational stability analysis on Eqs. (4.10) and (4.11), leads to the following dispersion relation:

$$\frac{\epsilon_1}{\cos\theta}\omega^3 + (1 - \epsilon_2\kappa)\omega^2 + \frac{\epsilon_1 \sin^2\theta}{\cos\theta}(2\sigma|b_0|^2 - K^2\sin^2\theta)\omega - \sin^2\theta[K^2\sin^2\theta - \epsilon_2\kappa(K^2\sin^2\theta - 2\sigma|b_0|^2)] = 0\ , \quad (4.12)$$

where the same notations as in Sec. II are used and $\omega = \Omega/K$. In Fig. 3, we display the dominant growth rate (imaginary part of ω) as a function of θ for $\sigma = \kappa = -1$, $\epsilon_1 = 0.05$, and $\epsilon_2 = 0.01$. The thickness of the unstable boundary layer at $\theta = \pi/2$ is independent of ϵ_2 and roughly proportional to $1/\epsilon_1$. The other instability region spreads towards larger angles as ϵ_2 increases or ϵ_1 decreases. For $\sigma = -1$ and $\kappa = +1$, the instability is restricted to a boundary layer close to $\theta = \pi/2$. The parameter κ thus plays an important role, although it appears multiplied by the small quantity ϵ_2. Indeed, for $\epsilon_2 = 0$, the nonlinear term disappears in the adiabatic limit. According to its sign, the $\epsilon_2\kappa$ correction in Eq. (4.11), which originates from the difference between the group and the phase velocity of the Alfvén wave, corresponds to a focusing or defocusing nonlinearity.

For $\sigma = +1$, the stability results are similar to those discussed above when $\sigma\kappa$ is the same, except that no boundary layer arises near $\theta = \pi/2$. We conclude that in the limit $\xi \to 0$, the stability properties of Eqs. (4.10)

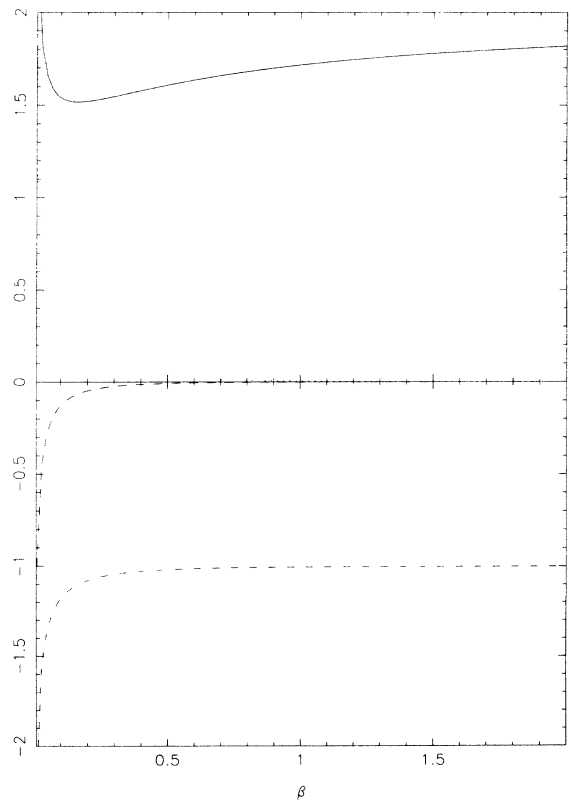

FIG. 2. Variation with β of the coefficients λ_1 (dashed-dotted line), λ_2 (dotted line), μ_1 (solid line) and μ_2 (dashed line) defined in Eqs. (4.5)–(4.8).

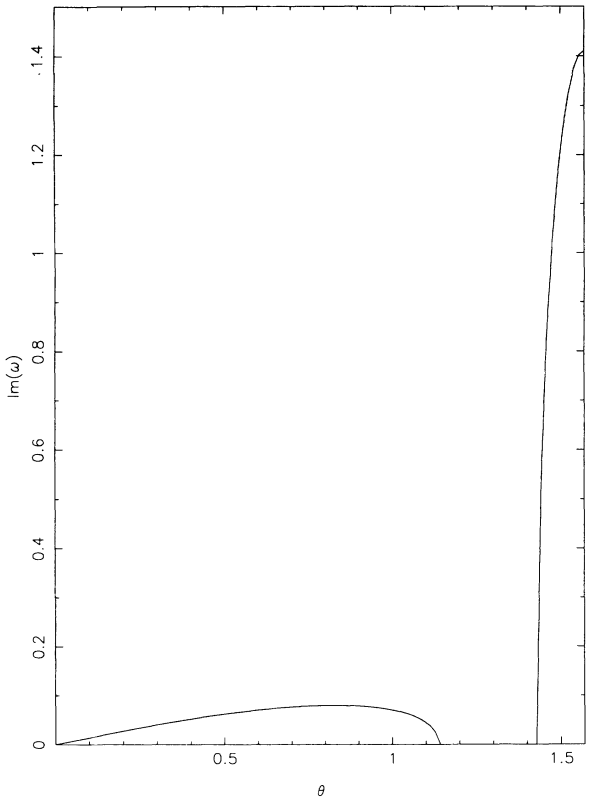

FIG. 3. Dominant growth rate as a function of θ for a right-hand carrying Alfvén wave ($\kappa < 0$) and $\beta > 1$.

and (4.11) identify qualitatively with those of the complete system (2.9)–(2.12).

V. NONLINEAR DYNAMICS IN THE DISPERSIONLESS LIMIT

This section is devoted to the numerical integration of Eqs. (4.1) and (4.2) when $\sigma = -1$. The case $\sigma = +1$ is essentially defocusing. In order to ensure accuracy, we use the anisotropic dynamic rescaling method developed in the context of the nonlinear Schrödinger equation [16]. For simplicity, we concentrate on solutions which are axisymmetric in the transverse variables. We write

$$B(x,y,z,t) = \frac{1}{S(t)}\Psi(\xi_1,\xi,\tau) \tag{5.1}$$

$$W_i(x,y,z,t) = \frac{1}{S^2(t)}\phi_i(\xi_1,\xi,\tau) \quad (i=1,2) \tag{5.2}$$

in terms of the stretched variables $\xi_1 = \frac{x}{s_1(t)}$, $\xi = \frac{\sqrt{y^2+z^2}}{s(t)}$, $\tau = \int_0^t \frac{1}{S^2(u)}du$, where the scaling factors $s_1(t)$, $s(t)$, $S(t)$ will be prescribed later. A translation of the origin of the coordinates (especially in the x direction) and a rotation of the coordinate axes could be included in this formalism, but do not appear to be necessary in the present context. Substituting in Eqs. (4.1) and (4.2), we get ($i = 1, 2$)

$$\frac{1}{i}\left(\partial_\tau\Psi + a\xi\partial_\xi\Psi + a_1\xi_1\partial_{\xi_1}\Psi - \frac{S_\tau}{S}\Psi\right) + \frac{S^2}{s^2}\Delta_\perp\Psi + (|\Psi|^2 + \phi_1 + \phi_2)\Psi = 0, \tag{5.3}$$

$$\eta\left(\partial_\tau\phi_i + a\xi\partial_\xi\phi_i + a_1\xi_1\partial_{\xi_1}\phi_i - 2\frac{S_\tau}{S}\phi_i\right) + (\lambda_i + \eta\kappa)\frac{S^2}{s_1}\partial_{\xi_1}\phi_i = \frac{S^2}{s_1}\mu_i\partial_{\xi_1}|\Psi|^2, \tag{5.4}$$

where

$$a = -\partial_\tau \ln|s| \,, \qquad a_1 = -\partial_\tau \ln|s_1| \,. \tag{5.5}$$

In order to keeps all the terms of the same order in the rescaled equations, we require

$$\frac{2}{s^2} + \frac{1}{s_1} = \frac{3}{S^2} \,. \tag{5.6}$$

We also define the normalized scaling factors

$$l^2 = \frac{2}{3}\frac{S^2}{s^2} \,, \qquad l_1^2 = \frac{1}{3}\frac{S^2}{s_1} \,. \tag{5.7}$$

Furthermore, we prescribe that in the rescaled variables, the magnetic field keep a constant scale in both the longitudinal and transverse directions, in the form

$$\frac{\int \xi_1^2|\Psi|^{2p}\xi d\xi d\xi_1}{\int |\Psi|^{2p}\xi d\xi d\xi_1} = 1 \,, \qquad \frac{\int \frac{\xi^2}{2}|\Psi|^{2p}\xi d\xi d\xi_1}{\int |\Psi|^{2p}\xi d\xi d\xi_1} = 1 \tag{5.8}$$

which corresponds to ($r = \sqrt{y^2+z^2}$)

$$s_1^2 = \frac{\int x_1^2|B|^{2p}rdrdx}{\int |B|^{2p}rdrdx} \,, \qquad s^2 = \frac{1}{2}\frac{\int r^2|B|^{2p}rdrdx}{\int |B|^{2p}rdrdx} \,. \tag{5.9}$$

In our numerical simulations, we use $p = 3$. Differentiating (5.9) with respect to time and using Eqs. (5.3) and (5.4), we obtain

$$a_1 = \frac{3}{2}pl_1^2\frac{\int(1-\xi_1^2)\Im(\Delta_\perp\bar\Psi\Psi)|\Psi|^{2(p-1)}\xi d\xi d\xi_1}{\int |\Psi|^{2p}\xi d\xi d\xi_1}, \tag{5.10}$$

$$a = \frac{3}{2}pl^2\frac{\int(1-\frac{\xi^2}{2})\Im(\Delta_\perp\bar\Psi\Psi)|\Psi|^{2(p-1)}\xi d\xi d\xi_1}{\int |\Psi|^{2p}\xi d\xi d\xi_1} \,. \tag{5.11}$$

Furthermore, we easily check that, from (5.6),

$$\frac{S_\tau}{S} = -\left(l^2a + \frac{1}{2}l_1^2a_1\right) \tag{5.12}$$

and from (5.7)

$$\frac{1}{l^2}\frac{dl^2}{d\tau} = -2\left(al^2 + \frac{a_1}{2}l_1^2\right) + 2a, \tag{5.13}$$

$$\frac{1}{l_1^2}\frac{dl_1^2}{d\tau} = -2\left(al^2 + \frac{a_1}{2}l_1^2\right) + a_1 \,, \tag{5.14}$$

which close the system.

The coupled equations (5.3) and (5.4), (5.12)–(5.14) are solved numerically by a second-order finite difference method. The ξ variable which extends from 0 to ∞, is mapped to a finite interval using an homographic mapping, while the ξ_1 variable is restricted to the interval $[-30, 10]$. We use a resolution of 400 grid points in the x direction and 200 in the r direction. The initial conditions are fixed as $B = 4e^{-r^2-x^2}$ and $W_1 = W_2 = 0$. As the integration proceeds, the original fields $B(x,r,t)$, $W_1(x,r,t)$, and $W_2(x,r,t)$ are reconstructed from the scaling factors and the rescaled profiles.

We checked that the wave W_2 is indeed negligible for $\beta > 1$, its amplitude remaining smaller than the other wave by a factor of order μ_2/μ_1. It is thus convenient to describe the results of the simulations in terms of the parameters ϵ_1 and ϵ_2 entering Eqs. (4.10) and (4.11) and to write $W_1 = W$.

Figure 4 displays the longitudinal variation of $|B|$ and W at $r = 0$ and various times, for $\epsilon_1 = 0.11$ and $\kappa\epsilon_2 = -1.7 \times 10^{-3}$. At early times when W is negligible, we observe the onset of radial focusing, leading to a moderate growth of the maximum of $|B|$. Meanwhile, W develops a mostly antisymmetric profile [Fig. 4(a)]. We then observe a shift of the focus in the negative x direction towards which the wave propagates. Later on, as seen in Fig. 4(b), the initial x symmetry of $|B|$ is broken and W displays a sharp front. The maximum of $|B|$ then starts decreasing and W develops a symmetric component [Fig. 4(c)]. At this time, the $|B|$ peak splits and ejects a fraction of its energy towards the negative x. The radial L_2 norm then becomes subcritical and the collapse is arrested. While the magnetic field envelope defocuses and spreads in the radial direction, an intense sonic wave displaying a sharp front propagates away from the magnetic pulse [Figs. 4(d)]. Reminding that in the present asymptotics (such as for the DNLS equation), the amplitude of the sonic wave is second-order compared to that of the transverse magnetic field, we find that, even though the amplitude of $|B|$ has decreased, a strong amplification of W may question this scaling.

In order to address the effect of the longitudinal scale (in the x direction) of the initial modulation, we vary the parameter ϵ_1. When we decrease this scale by taking $\epsilon_1 = 3.7 \times 10^{-2}$, we still observe an inhibition of the collapse but the evolution is different. At early times [Fig. 5(a)], W still displays the antisymmetry of the spatial

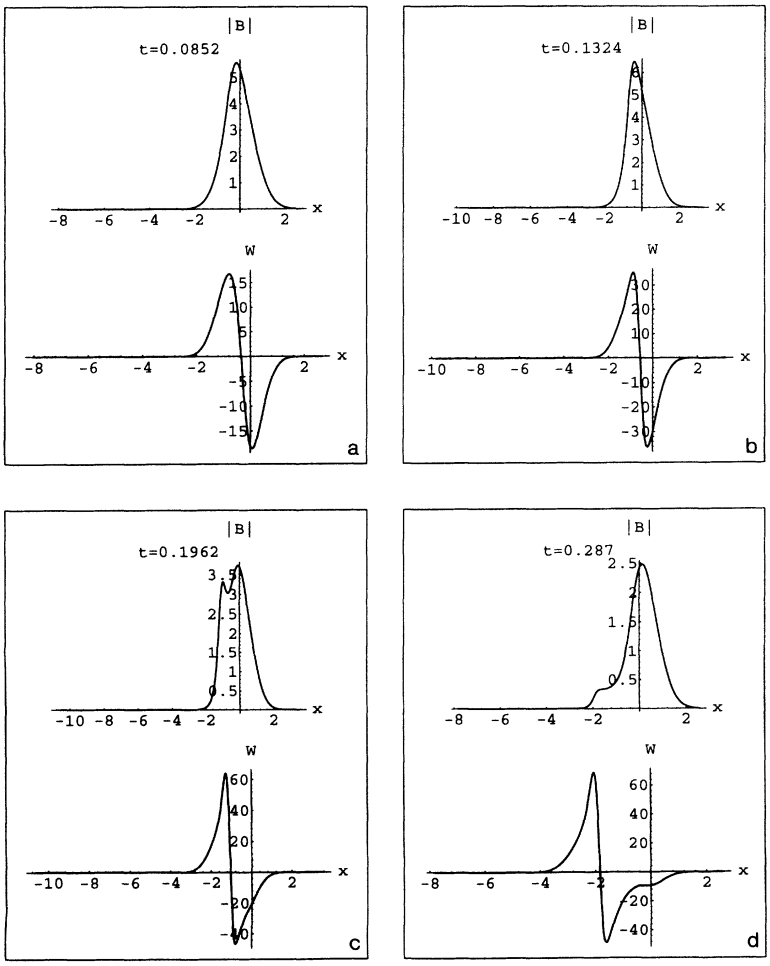

FIG. 4. Longitudinal variation of the Alfvén wave envelope $|B|$ and of the sonic wave W, given by Eqs. (4.1) and (4.2), for $\epsilon_1 = 0.11$ and $\kappa\epsilon_2 = -1.7 \times 10^{-3}$, at $r = 0$ and various times.

contribution of the ponderomotive force, but rapidly, the positive and negative parts separate. The positive part moves towards negative x, while the negative one stays at the location of the $|B|$ pulse and tends to relax to its adiabatic limit $-|B|^2$, resulting in a strong inhibition of the focusing [Fig. 5(b)]. Figures 5(c) and 5(d) display at the same times as Figs. 5(a) and 5(b), respectively, the radial profile of $|B|$ and W at the point of the x axis where $|B|$ is maximum. We observe that both the longitudinal and transverse scales had not significantly changed since the initial time.

On the other hand, if we consider a longitudinal modulation at a much larger scale, taking $\epsilon_1 = 0.56$, the behavior is radically different and far from the adiabatic limit. In this case, the collapse is not arrested. For slightly negative x, both the magnetic field envelope and the sonic wave become very intense and a sharp sonic front develops [Fig. 6(a)]. Figure 6(b) displays the radial profile of $|B|$ and $|W|$ at locations on the x axis where their amplitudes are maximum. Comparing with Fig. 6(a), it is clear that although the characteristic scale in the x direction has slightly decreased, it remains much larger than the radial scale, indicating the formation of a filament with a finite longitudinal extent.

We now investigate the influence of the parameter ϵ_2, measuring the ratio between the Alfvén wavelength and the ion gyromagnetic radius. Here we fix $\epsilon_1 = 0.11$ but for an easier understanding of the dynamics, we do not restrict ϵ_2 to the very small values required by the DNLS asymptotics. For $\epsilon_2\kappa = -0.41$ or $\epsilon_2\kappa = -0.69$, the collapse is arrested but the behavior of W is different from the case where ϵ_2 is much smaller. The positive and negative parts of W separate, a positive bump being ejected towards the negative x and a negative bump staying at the pulse location. For $\epsilon_2\kappa = -1.5$, the W field is not large enough to arrest the collapse and the focusing goes on, while the wave takes a symmetric form at the location of the B peak as shown in Fig. 7. In this case, the longitudinal scale has slightly increased. If now, changing the sign of κ, we take $\epsilon_2\kappa = 0.72$, focusing takes place, while the trapped wave depicts an antisymmetric profile (Fig. 8). It is noticeable that, while the longitudinal $|B|$ profile smoothly decreases towards the positive x values, a sharp front appears on the negative side, corresponding to an asymmetry of the filament intensity along the x axis. The transition between the non-focusing and focusing dynamics probably occurs near $\epsilon_2 = 0.44$, for which the simulation we have performed does not allow us to decide about a possible collapse.

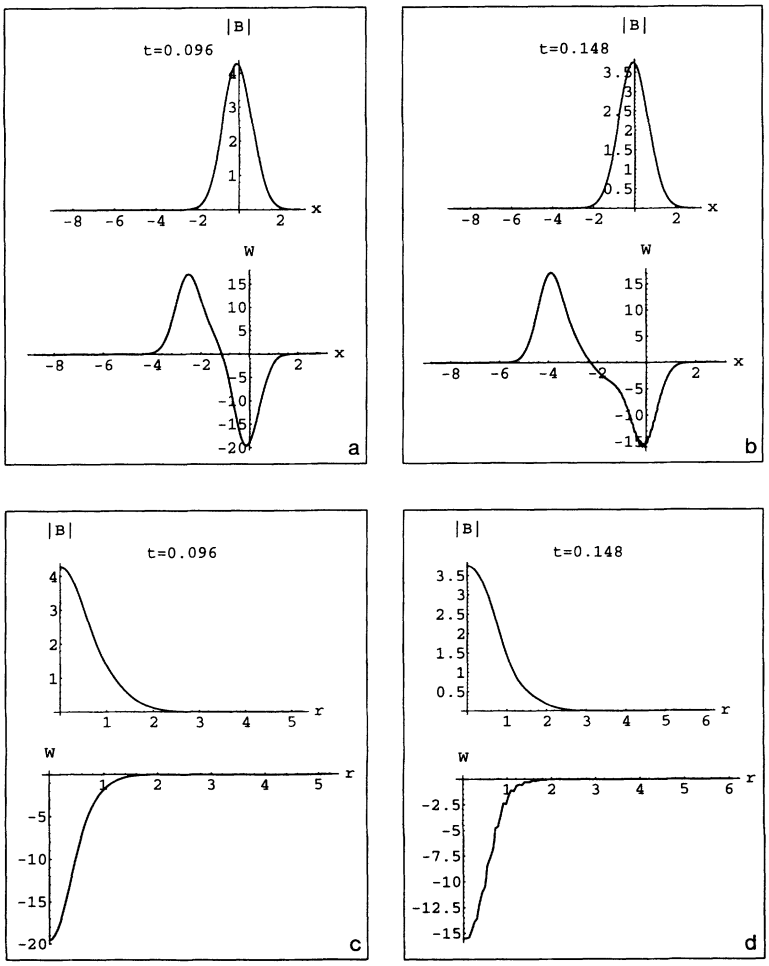

FIG. 5. Variation of $|B|$ and W in the longitudinal direction at $r = 0$ (a, b), and in the radial direction at $x = 0$ (c, d), at two different times, for $\epsilon_1 = 3.7 \times 10^{-2}$ and $\kappa\epsilon_2 = 3.7 \times 10^{-2}$.

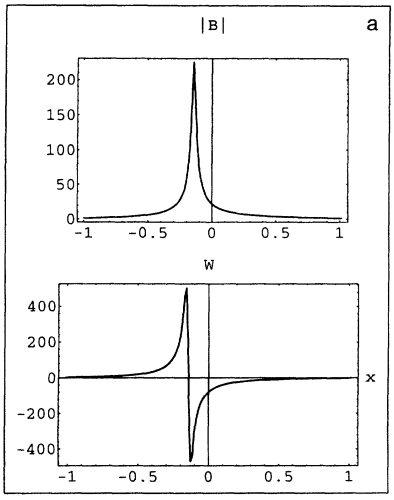

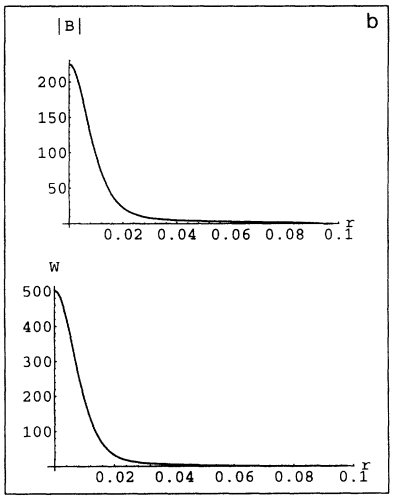

FIG. 6. Variation of $|B|$ and W in the longitudinal direction at $r = 0$ (a), and in the radial direction at the point of the x axis where they are maximum (b), for $\epsilon_1 = 0.56$ and $\kappa\epsilon_2 = -1.7 \times 10^{-3}$.

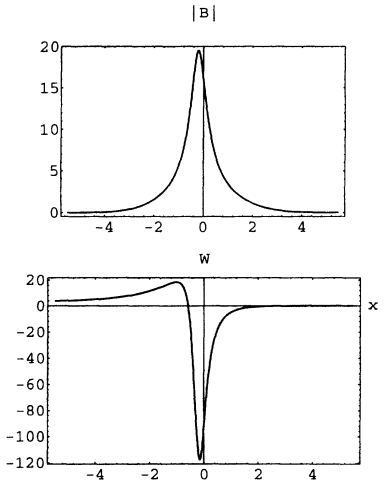

FIG. 7. Variation of $|B|$ and W in the longitudinal direction at $r = 0$, for $\epsilon_1 = 0.11$ and $\kappa\epsilon_2 = -1.5$.

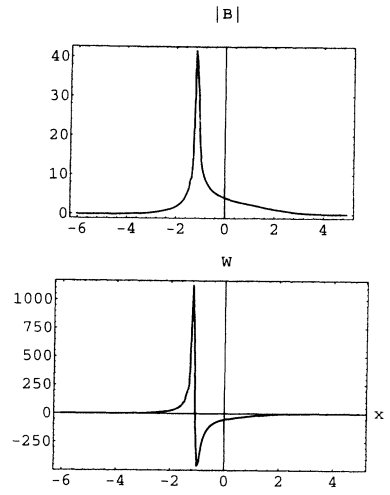

FIG. 8. Same as Fig. 7, for $\epsilon_1 = 0.11$ and $\kappa\epsilon_2 = 0.72$.

VI. THE MECHANISM OF FOCUS INHIBITION

In this section, proceeding in the spirit of Ref. [11], we analyze in the context of Eqs. (4.10) and (4.11), how sonic waves can in some instances inhibit the Alfvén wave focusing. We assume that W is initially zero and that, for a while, the B field develops a radial focus in independent x planes of the form

$$|B|^2(x,r,t) = a(x)f(t_\star(x) - t) \times R\{b(x)f(t_\star(x) - t)r\}, \tag{6.1}$$

where $t_\star$ denotes the x-dependent singularity time, while $a(x)$ and $b(x)$ are smooth and finite rescaling factors. Up to logarithmic corrections, the function $f(t_\star(x) - t)$ behaves like $[t_\star(x) - t]^{-1/2}$. Close to the singularity, the variation in the x direction is thus strongly dominated by the dependence on $t_\star(x)$. Near the focusing, we are thus led to write

$$|B|^2(x,r,t) \approx \mathcal{G}(t_\star(x) - t, r) \ . \tag{6.2}$$

Equation (4.11) is then solved along the characteristics $x(t) = -\frac{c}{\epsilon_1}t + x_0$ in the form

$$W(x(t),t) = \frac{1}{\epsilon_1}\int_0^t \partial_X |B|^2[x(\tau),\tau]d\tau \ , \tag{6.3}$$

where the r dependence has been omitted. Using Eq. (6.2), we write

$$W(x(t),t) = \frac{1}{\epsilon_1}\int_0^t t'_\star(x(\tau))\frac{d\mathcal{K}}{du}d\tau \ , \tag{6.4}$$

where $\mathcal{K}\{\tau\} = \mathcal{G}(t_\star(x(\tau)) - \tau\}$ and $u = t_\star(x(\tau)) - \tau$. This leads to

$$W(x(t),t) = -\frac{1}{\epsilon_1}\int_0^t \frac{t'_\star(x(\tau))}{1 + \frac{c}{\epsilon_1}t'_\star(x(\tau))}\frac{d\mathcal{K}}{d\tau}d\tau \ . \tag{6.5}$$

Integrating by part, we obtain

$$W(x,t) = \frac{-\frac{t'_*(x)}{\epsilon_1}}{1+\frac{c}{\epsilon_1}t'_*(x)}|B|^2(x,t) + \frac{\frac{t'_*(x_0)}{\epsilon_1}}{1+\frac{c}{\epsilon_1}t'_*(x_0)}|B|^2(x_0,0) + \int_0^t \frac{d}{d\tau}\left(\frac{\frac{t'_*(x(\tau))}{\epsilon_1}}{1+\frac{c}{\epsilon_1}t'_*(x(\tau))}\right)\mathcal{H}d\tau \,. \quad (6.6)$$

The second term on the right-hand side of this equation is negligible compared to the first one near the focusing. The last one can be estimated using the intermediate value theorem [since $t''_*(x)$ is positive near the maximum of the peak], as a term proportional to $|B|^2[x(\theta t),\theta t]$ with $0<\theta<1$. The nonlinear term in Eq. (4.10) then reduces to

$$(W+|B|^2)B \approx \frac{1+(c-1)\frac{t'_*(x)}{\epsilon_1}}{1+c\frac{t'_*(x)}{\epsilon_1}}|B|^2B \quad (6.7)$$

since $|B|^2[x(\theta t),\theta t]B(x(t),t)$ is very small near the collapse (provided θ is not close to 1).

Equation (6.7) enables us to predict the effect of the sonic wave when it begins to react on the magnetic field, and to interpret the numerical results presented in Sec. IV. When $\epsilon_1 \ll c$, we recover the adiabatic limit governed by the sign of $(c-1)/c$. Indeed, for $c<1$, defocusing occurs, while for $c>1$, the collapse proceeds with $W=-|B|^2$. When c is of order ϵ_1 (assumed to be small), the situation is more complex. Recalling that $t'_*(x)$ is finite and negative (assuming c is positive), we see that the nonlinear term has the sign of $1+\frac{c}{\epsilon_1}t'_*(x)$, and thus can be negative (defocusing case) if c is large enough compared to ϵ_1, or positive (focusing case) otherwise. In the latter case, the W profile is mainly dominated by its antisymmetric component, as can be seen from Eq. (6.6), where $t'_*(x)$ is itself antisymmetric. Finally, for ϵ_1 very large (corresponding to almost purely transverse perturbations), the wave W is antisymmetric and the collapse is not arrested.

VII. CONCLUDING REMARKS

In this paper, we discussed the effect of slow longitudinal modulations on the filamentation of a circularly polarized Alfvén wave. This perturbation is singular due to the existence of a mean flow driven by magnetosonic waves, whose influence decreases with the scale of the longitudinal perturbation. In the context of the linear modulational stability analysis, it is shown that no filamentation occurs for $\beta<1$, suggesting that in supersonic and sub-Alfvénic regimes, Alfvén waves of moderate amplitude propagating along the ambient magnetic field, can survive and do not evolve into a much stronger nonlinear regime. On the other hand, for $\beta>1$, the mean flow induces an instability confined in an angular boundary layer corresponding to quasitransverse perturbations. However, due to the coexistence of stability and instability regions depending on the orientation of the perturbation wave vector, an understanding of the dynamics requires the resolution of the fully nonlinear equations. Their numerical integration showed that magnetosonic waves can arrest the collapse when their scale and/or their speed with respect to the Alfvén group velocity, is not too large. Nevertheless, the dynamics generates sharp fronts for the sonic waves or density clump shifted with respect to the peak Alfvén wave intensity. In this situation, a significant amount of energy is transferred from Alfvén waves to localized density fluctuations by a nondissipative mechanism. In contrast, when density fronts are produced, dissipation will occur at the locations of the early time focus. This provides a new mechanism for shock formation, different from the one proposed in the context of the Cohen-Kulsrud-Burgers equation discussed in Ref. [18], without referring to transverse propagation effects [19]. The precise description of this regime may require one to go back to the multidimensional DNLS equations derived in Ref. [4], and possibly to include nonlinearities in the sonic waves evolution [20].

ACKNOWLEDGMENTS

The numerical simulations were performed on the CRAY-YMP computers of the Institut Méditerranéen de Technologie (Marseille) and of CRAY Research Inc. (Eagan, Minnesota). This work benefited from support by NSERC Operating Grant No. OGPIN16 and from the European Cooperative Network "Numerical Simulations of Nonlinear Magnetohydrodynamic Phenomena" (ERBC HRXCT930410).

[1] F.H. Shu, F.C. Adams, and S. Lizano, Ann. Rev. Astron. Astrophys. **25**, 23 (1987).

[2] S. Spangler, S. Fuselier, A. Fey, and G. Anderson, J. Geophys. Res. **93**, No. A2, 845 (1988).

[3] V.E. Zakharov and A.M. Rubenchik, Prikl. Mat. Techn. Fiz. **5**, 84 (1972); V.E. Zakharov and E.I. Schulman, in *What is Integrability?*, edited by V.E. Zakharov, Springer Series on Nonlinear Dynamics (Springer-Verlag, Berlin, 1991), pp. 185–250.

[4] T. Passot and P.L. Sulem, Phys. Rev. E **48**, 2966 (1993).

[5] E. Mjølhus and J. Wyller, Phys. Scr. **33**, 442 (1986); J. Plasma Phys. **40**, 299 (1988).

[6] C.R. Ovenden, H.A. Shah, and S.J. Schwartz, J. Geophys. Res. **88**, 6095 (1983).

[7] M.J. Ablowitz, S.V. Manakov, and C.L. Schultz, Phys. Lett. A **148**, 50 (1990); M.J. Ablowitz and P.A. Clarkson, *Solitons, Nonlinear Evolution Equations and Inverse Scattering*, London Mathematical Society Note Series 149

(Cambridge University Press, Cambridge, 1991).
[8] S.P. Kuo, M.H. Whang, and M.C. Lee, J. Geophys. Res. **93**, 9621 (1988).
[9] P.K. Shukla and L. Stenflo, Astrophys. Space Sci. **155**, 145 (1989).
[10] P.K. Shukla, G. Feix, and L. Stenflo, Astrophys. Space Sci. **147**, 383 (1988).
[11] G.G. Luther, A.C. Newell, and J.V. Moloney, Physica D (to be published).
[12] G.C. Papanicolaou, C. Sulem, P.L. Sulem, and X.P. Wang, Physica D **72**, 61 (1994).
[13] J.M. Ghidaglia and J.C. Saut, Nonlinearity **3**, 475 (1990).
[14] F. Linares and G. Ponce, Ann. Inst. Henri Poincaré Analyse non Linéaire **10**, 523 (1993).
[15] E. Mjølus and T. Hada, J. Plasma Phys. **43**, 257 (1990).
[16] M.J. Landman, G.C. Papanicolaou, C. Sulem, P.L. Sulem, and X.P. Wang, Physica D **47**, 393 (1991).
[17] H. Washimi and V.I. Karpman, Zh. Eksp. Teor. Fiz. **71**, 1010 (1976) [Sov. Phys. JETP **44**, 528 (1976)].
[18] M.A. Malkov, C.F. Kennel, C.C. Wu, R. Pellat, and V.D. Shapiro, Phys. Rev. B **3**, 1407 (1991).
[19] S. Spangler and B.B. Plapp, Phys. Fluids B **4**, 3356 (1992).
[20] T. Hada, Geophys. Res. Lett. **20**, 2415 (1993).